# Fracture behavior of tungsten-based composites exposed to steady-state/transient hydrogen plasma

**Y. Li**[1,2,3], **T.W. Morgan**[1] , **J.A.W. Van Dommelen**[2] , **S. Antusch**[4], **M. Rieth**[4] , **J.P.M. Hoefnagels**[2] , **D. Terentyev**[5], **G. De Temmerman**[6] , **K. Verbeken**[3] **and M.G.D. Geers**[2]

[1] DIFFER-Dutch Institute for Fundamental Energy Research, De Zaale 20, 5612 AJ, Eindhoven, Netherlands

[2] Department of Mechanical Engineering, Eindhoven University of Technology, 5600 MB, Eindhoven, Netherlands

[3] Department of Materials, Textiles and Chemical Engineering, Ghent University (UGent), Technologiepark 46, B-9052, Ghent, Belgium

[4] Karlsruher Institut für Technologie (KIT), 76021, Karlsruhe, Germany

[5] SCK·CEN, Nuclear Materials Science Institute, Boeretang 200, 2400, Mol, Belgium

[6] ITER Organization, Route de Vinon sur Verdon, CS 90 046, 13067, St Paul Lez Durance Cedex, France

E-mail: Y.Li@differ.nl

## Abstract

The fracture behavior of plasma-facing components (PFCs) under extreme plasma-material interaction conditions is of great concern to ITER and future fusion reactors. This was explored in the current study by exposing pure tungsten (W), W-1%TiC and W-2%$Y_2O_3$ composites to a combined steady-state/transient hydrogen plasma up to a base surface temperature of ~2220 K, and up to 5000 transient pulses for 1000 s using the linear plasma generator Magnum-PSI. The applied heat loads were characterized by combining sheath physics, thermographic information and finite element analyses, with which the thermal stress was evaluated. Combining microstructural investigation and thermo-mechanical numerical analyses, a physical picture of fracture is developed. The transient heat loads drive surface crack initiation, whose depth can be estimated by a simple analytical model for pure tungsten, while the cooling period following the steady-state heat load induces tensile stresses, opening existing surface cracks deeper. The fracture process is mediated by the microstructure whereby the ceramic particles stabilize the microstructure but promote surface crack initiation due to suppressed plasticity at the grain boundaries and the particle-matrix interfaces. The surface cracks relieve the subsequent cycles of transient thermal stress but intensify the steady-state thermal stress, therefore, promoting deep crack propagation. These results help to understand failure mechanisms in PFCs under extreme operation conditions which are valuable for developing advanced PFCs.

Keywords: tungsten, composites, edge localized modes (ELMs), hydrogen plasma, recrystallization, fracture

## 1. Introduction

Designing divertor plasma-facing components (PFCs) which can withstand the extreme particle and heat loads expected in a fusion reactor is a challenging task. Recrystallization is known to strongly modify the materials' mechanical response, e.g. by reducing yield strength and enhancing ductility, as empirically described by the Hall-Petch relationship [1]. Contrary

to most metals, recrystallization may decrease the ductility of tungsten, which is attributed to the diminished fraction of low angle grain boundaries and edge dislocation density after recrystallization [2]. Although the role of recrystallization on the performance of PFCs is complicated and also has positive effects (for example by annealing neutron radiation damage [3]), undesirable deterioration of the thermal shock resistance has generally been observed [4, 5]. For the current ITER monoblock design, in order to avoid recrystallization (identified through a hardness drop of 50%) of the 2 mm surface layer during the first divertor lifetime high performance exposure, the steady-state heat flux is limited to ~$16 \pm 2.5$ MWm$^{-2}$ [6], which might be surpassed in a future fusion reactor such as DEMO. Thermal stress due to steady-state and transient heat loads can drive crack initiation and propagation due to high cycle fatigue, even when individual events are not capable of immediately inducing cracking [7]. In ITER, a large number of mitigated edge localized modes (ELMs) are expected [8] and fatigue effects leading to damage accumulation over time have been observed for cyclic electron-beam loading of tungsten under ITER-relevant conditions [9, 10]. An additional factor is that hydrogen is known to cause degradation of the fracture toughness in metallic materials, classically termed as hydrogen embrittlement (HE) [11]. A high flux (~$10^{24}$ m$^{-2}$ s$^{-1}$) hydrogen plasma environment, as expected in the ITER divertor regime, therefore may induce an additional degradation factor affecting the materials' performance and lifetime.

Tungsten produced by conventional powder metallurgy is the current solution for ITER [12]. Meanwhile, various tungsten-based composites are under development with reported improvements in particular aspects [13–17], with the general design principle being retarding recrystallization and preventing crack propagation by incorporating ceramic particles. One particular fabrication method is powder injection molding (PIM), which has the advantage of mass production of low cost, high-performance components with complex geometries, which also enables easy incorporation of ceramic particles into the metal matrix [18]. The performance of such composites under a combination of high particle/heat flux, a high surface temperature, and high ELM-cycle numbers remains to be assessed.

Such experimental studies are readily enabled by the linear plasma generator Magnum-PSI, designed to study plasma-wall interactions in ITER-like divertor regimes [19, 20]. Despite numerous experimental and numerical studies [4, 9, 10, 21–34] that contributed to our understanding of the plasma-material interactions, the physical picture of fracture under the aforementioned conditions is still incomplete. Experimentally, most devices can only probe part of the parameters, and thus the synergetic effects in the real heat and particle loading regime cannot be fully captured [35]. For numerical models, experimental validation data (e.g. high-fidelity experimental input and output for the thermo-mechanical problem) is generally lacking such that the predictive value of the results is limited. Because of these limitations, in this study, we exploit the advanced diagnostics information in Magnum-PSI in combination with a numerical model and adequate post-mortem microstructural characterization, to obtain a physical

picture of fracture, with insights into the crack initiation and propagation process and their interplay with the underlying microstructures.

The paper is organized as follows. In section 2, the experimental procedure including sample preparation, plasma exposure, and diagnostics is detailed. The Bohm sheath theory used to determine particle flux and steady-state heat flux is then shortly summarized. A procedure combining experimental thermographic information and finite element method (FEM) analyses is also developed to derive the transient heat flux reaching the targets. The resulting microstructure is analyzed in section 3, with an emphasis on crack initiation and propagation. In section 4, the observed results are discussed with the help of additional thermal stress calculations.

## 2. Experimental and numerical procedures

### 2.1. Specimen preparation

W-1%TiC and W-2%Y$_2$O$_3$ samples ($10 \times 10 \times 1$ mm$^3$) were produced by powder injection molding at KIT [36], while hot-rolled polycrystalline tungsten discs (20 mm diameter, 1 mm thickness) with a purity of 99.97 wt.% were produced by Plansee SE. The geometry of the samples is not identical, but the thickness is the same, which is considered to be the controlling geometrical factor influencing damage/crack formation. The samples were first ground with SiC papers up to #2000 and then polished with 3 $\mu$m and 1 $\mu$m diamond suspension, respectively. Thereafter they were ultrasonically cleaned in acetone and ethanol for 30 min followed by stress relief annealing at 1000 °C at a pressure below $1 \times 10^{-4}$ Pa for 1 h. To further remove residual stresses from the previous steps, as noted in [37, 38], electropolishing was conducted using a 0.4% g ml$^{-1}$ aqueous NaOH solution at a voltage of 15 V and at a current density ~191 A m$^{-2}$. The erosion rate was around 3.68 nm s$^{-1}$, estimated by Faraday's law of electrolysis. Based on this erosion rate, pure tungsten samples were electropolished to a depth of 1 $\mu$m, while PIM tungsten-based composites were electropolished to a depth of 100 nm to avoid removing ceramic particles.

### 2.2. Plasma exposure

Hydrogen plasma exposures were performed in the linear plasma generator Magnum-PSI. The steady-state plasma was generated by a cascaded arc source using a DC current of 180 A, an H$_2$ gas flow in the range 14–18 Pa · m$^3$ s$^{-1}$ and delivered to the targets by applying a constant axial magnetic field of 1.2 T. Transient plasma pulses (~1 ms in duration) were superimposed on the steady-state plasma using the pulsed source system (described in [20]) with a stored energy in the capacitor of either 75 J or 192 J, with a pulse frequency of either 1 Hz or 5 Hz, respectively. The samples were clamped to a water-cooled copper holder with two GRAFOIL® layers in between using a TZM alloy clamping ring. All targets were kept at a floating potential, the electron temperature during steady-state plasma was ~1 eV and reached ~10 eV during pulses. The plasma loading parameters are summarized

in table 1, as determined from the methods discussed below. The particle/heat loads indicated in table 1 are measured at the center of the plasma beam, which has a Gaussian distribution profile in terms of electron temperature and density and a ~10 mm full-width half-maximum (FWHM), as measured by Thomson scattering. For the specimen's nomenclature: W, WY, WT stand for pure tungsten, W-2%$Y_2O_3$ and W-1%TiC, respectively.

## 2.3. Diagnostics and post-mortem analysis

The electron temperature ($T_e$) and density ($n_e$) of the plasma were measured by Thomson scattering (TS) at a position of ~30 mm in front of the targets [39]. $T_e$ and $n_e$ can also be determined at different points in a pulse using a triggering changing delay between the TS system and the pulsed plasma generation system, giving a time-resolved measurement of these parameters (described in [40]). The transient temperature excursions induced by the pulsed plasma were recorded by a fast-framing infra-red camera (FLIR SC7500MB) in the wavelength range of 3.97 to 4.01 $\mu$m and at a frequency of ~5 kHz. The temperature-dependent emissivity of tungsten was obtained by calibrating different base temperatures to that measured by a multi-wavelength pyrometer (FAR Associates FMPI). This was then used to convert the raw signal of the infra-red camera into temperature profiles using an in-house script, where the temperature-dependent emissivity was also considered during the temperature excursions.

The surface morphology of the samples was analyzed by a scanning electron microscope (SEM, JEOL 7500 FA, and Phenom), using a scanning voltage of 5 kV and secondary electron (SE) mode. It was carefully checked that the preparation of the cross-section did not alter the fracture morphology of the plasma-treated specimens in figure 5.

## 2.4. Thermal analysis

The heat flux on the target is calculated from sheath physics as follows:

$$q = \gamma k_B T_e \Gamma_i, \tag{1}$$

where $k_B$ is the Boltzmann constant, $T_e$ the electron temperature, $\Gamma_i$ the ion flux and $\gamma$ the so-called sheath heat transmission coefficient. The ion flux $\Gamma_i$ is determined by the ion density $n_{se}$ and velocity $v_{se}$ at the sheath edge, and can be expressed as:

$$\Gamma_i = n_{se} v_{se}. \tag{2}$$

The generalization of the non-zero ion temperature ($T_i$) Bohm criterion discussed by Riemann [41], yields the following expression of $v_{se}$:

$$v_{se} = \left[ (k_B T_e + \tfrac{5}{3} k_B T_i)/m_i \right]^{\frac{1}{2}}, \tag{3}$$

where $m_i$ denotes the mass of the ions and $\tfrac{5}{3}$ originates from the adiabatic flow with isotropic pressure assumption. For

hydrogen plasma in Magnum-PSI, $T_e = T_i$ is an adequate approximation, as previously measured by collective Thomson scattering [42]. The value of $n_{se}$ is smaller than the ion density measured upstream ($n_e$). In the case of a steady-state plasma, as measured in [43], an ion density drop by a factor of 2 is a good approximation, such that,

$$n_{se} = \tfrac{1}{2} n_e, \tag{4}$$

Finally, following the analysis in [44], the sheath heat transmission coefficient $\gamma$ is given by the following expression:

$$\gamma = (2.5 - eV_s - eV_{ps})(1 - R_{i,E}) + \frac{\chi_i}{k_B T_e} + \frac{\chi_r}{k_B T_e}(1 - R_{i,N})$$
$$+ \frac{2}{1 - \delta}(1 - R_{e,E}), \tag{5}$$

in which the first term represents the kinetic energy of the ions impinging on the target taking into account the drifting Maxwellian velocity distribution for the ions in the plasma and the acceleration over the pre-sheath and sheath towards the surface. The factor 2.5 is the average fluid velocity of the ions. The energy gained in the potential drop of the pre-sheath and sheath is $eV_{ps}$ ($\sim$0.7) and $eV_s$ ($\sim$2.5), respectively. $R_{i,E}$ is the ion energy reflection coefficient, to allow for ion back-scattering. The second term represents the contribution from electron-ion recombination, with $\chi_i$ being 13.6 eV for hydrogen. The third term accounts for the atom-atom recombination energy $\chi_r$ (2.2 eV for hydrogen), for which ion particle reflection is also allowed for by $R_{i,N}$. Lastly, the energy deposited by electrons is considered, where $R_{e,E}$ is the electron energy reflection coefficient and $\delta$ is the secondary electron emission yield. We use $R_{i,E} = 0.3$, $R_{i,N} = 0.5$, $R_{e,E} = 0.15$ and $\delta = 0$ in this study, adopted from [44]. The steady-state heat flux can then be readily calculated from the measured $T_e$ and $n_e$ using equations (1)–(5). The results are summarized in table 1.

The electron temperature and density during pulsed plasma were also measured by our time-resolved Thomson scattering system, as shown in figure 1(a), averaged from 300 pulses. The $T_e$ variation was around 1 ms in duration with a peak temperature around 10 eV, while the density pulse was almost two times longer, rising to a maximum value and saturating there until $T_e$ drops again to a low value. This discrepancy in time evolution implies complex plasma surface interactions in the high-flux regime, which, as a direct consequence, also mediates the power deposition of plasma on the targets. As shown by Zielinski et al [45], the back-flow of neutrals from the target impedes the power transfer, resulting in a reduced heat flux. We also found that direct calculation by sheath theory using the above equations dramatically overestimated the heat flux received by the targets when comparing to analytical estimates using the measured peak surface temperature increase. To circumvent this complication, thermographic information coupled to FEM analysis was used to determine the actual heat flux. figure 1(b) shows a typical thermographic profile where the base temperature was measured by a pyrometer while the pulse events were captured by a fast-framing IR camera. Here, thermal equilibrium is reached after about 10 s and the stable

**Table 1.** Loading conditions of each sample in this study. W, WY, and WT stand for pure tungsten, W-2%Y$_2$O$_3$ and W-1%TiC, respectively. The ion flux and steady-state heat flux are calculated from the Bohm sheath theory using the measured TS data. The base surface temperature ($T_{base}$) is measured by a pyrometer and the peak temperature excursion ($\Delta T$) due to transient heat loads is recorded by a fast-framing infrared camera. The peak pulsed heat flux is calculated using FEM analysis. The samples are intentionally poorly cooled to reach high surface temperatures.

| Specimen | Ion flux ($\times 10^{24}$ m$^{-2}$ s$^{-1}$) | $T_{base}$ (K) | $\Delta T$ (K) | Pulses (#) | Steady-state heat flux (MW m$^{-2}$) | Peak pulsed heat flux (MW m$^{-2}$) |
|---|---|---|---|---|---|---|
| W1 | | | | | | |
| WY1 | | | | 1000 | | |
| WT1 | | | | | | |
| W2 | 0.80 ± 0.11 | 1788 ± 27 | 469 ± 21 | | 3.74 ± 0.33 | 600 |
| WY2 | | | | 5000 | | |
| WT2 | | | | | | |
| W3 | | | | | | |
| WY3 | 2.93 ± 0.07 | 2224 ± 23 | 359 ± 20 | 1000 | 13.31 ± 0.20 | 460 |
| WT3 | | | | | | |

temperature plateau at 11–15 s is used for calibration. Also, the pyrometer recording after 16 s looks similar to the values after the first pulse and is therefore not given to more clearly show the IR camera data. The thermographic profile consists of three stages: (1) ramp up to a steady-state temperature, which takes about 15 s; (2) discharge from capacitor banks, giving rise to temperature excursions, where each pulse lasts about 1 ms, (3) the temperature recovery to the base temperature before the next capacitor is triggered. The detailed temperature evolution during the millisecond pulsed plasma is better visible in figure 1(d) as red dots. It was constructed by firstly locating the peak of each individual pulse by a spline fitting and then aligning all the peak positions in the same time interval thus resulting in a statistically representative profile. In this way, the uncertainty in the recorded temperature data due to the imperfect synchronization of the capacitor banks and the finite time resolution of the IR camera can be reduced. The above three stages are replicated numerically using a FEM analysis by solving the following heat equation,

$$\rho c \dot{T} = \vec{\nabla} \cdot \left( \kappa \vec{\nabla} T \right), \quad (6)$$

where $T$ denotes the absolute temperature, $\rho$ the density, $c$ the specific heat capacity, $k$ the thermal conductivity and $\vec{\nabla}$ the spatial gradient operator.

The FEM analysis is performed in MSC.Marc/Mentat®. The geometry and mesh of the model are shown in figure 1(c), which consists of 4000 8-node cubic finite elements. The temperature-dependent thermal conductivity and heat capacity were taken from [46, 47], respectively. As boundary conditions, a Gaussian heat flux profile (10 mm full-width half-maximum) was applied on the top surface, while the bottom nodes were prescribed to have a uniform temperature. A steady-state thermal analysis (i.e. not including the first term in equation (6)) was firstly conducted to simulate stage (1). For this stage, the magnitude and spatial distribution of the Gaussian heat flux were calculated from $T_e$ and $n_e$ using sheath physics (equations (1)–(5)). The temperature at the back-side of the target was determined by matching the resulting top surface temperature to that from the pyrometer measurement and was then fixed in the subsequent transient simulation. Fixing this back-side temperature is motivated by the fact that the characteristic heat propagation zone (~0.2 mm, estimated from the 1D analytical solution of thermal diffusion) of the transient heat load due to a millisecond pulsed plasma is limited to the surface. Therefore, the transient heat load is unlikely to alter the bottom temperature established from the first steady-state stage. This steady-state analysis is essential since it determines the temperature distribution of the target prior to transient heat loads and subsequently dictates its temperature response. Secondly, pulsed heat loads were added to the model, therefore a transient analysis was carried out. The transient Gaussian heat flux has an approximately linear rise part, the rise time of which is prescribed by the discharge circuit [20] to be 0.24 ms . The magnitude and the decay part of the transient Gaussian heat flux (assuming the same plasma beam size as the steady-state case) were kept as fitting parameters, such that the resulting temperature response on the surface matches the temperature registered with the IR camera. This is shown in figure 1(d), where an adequate agreement between experimental measurements and FEM calculations was achieved. The resulting heat flux profile of the transient heat load is also depicted in the inset, which is triangular with a rise time of 0.24 ms and a decay time of 0.4 ms. The derived peak pulsed heat flux is reported in table 1. Finally, the surface temperature recovers the steady-state level once the transient heat load ends. The decay curve also matches well with the IR camera measurements, giving confidence in the above calculations, especially the assumption that the back-side temperature does not change upon receiving transient heat loads on the top surface. We have evaluated the influence of the uncertainties from the sheath theory and the plasma beam size, and the difference was found to be small. Although there still remain experimental measurement uncertainties, it is not expected that these affect the conclusions we will draw.
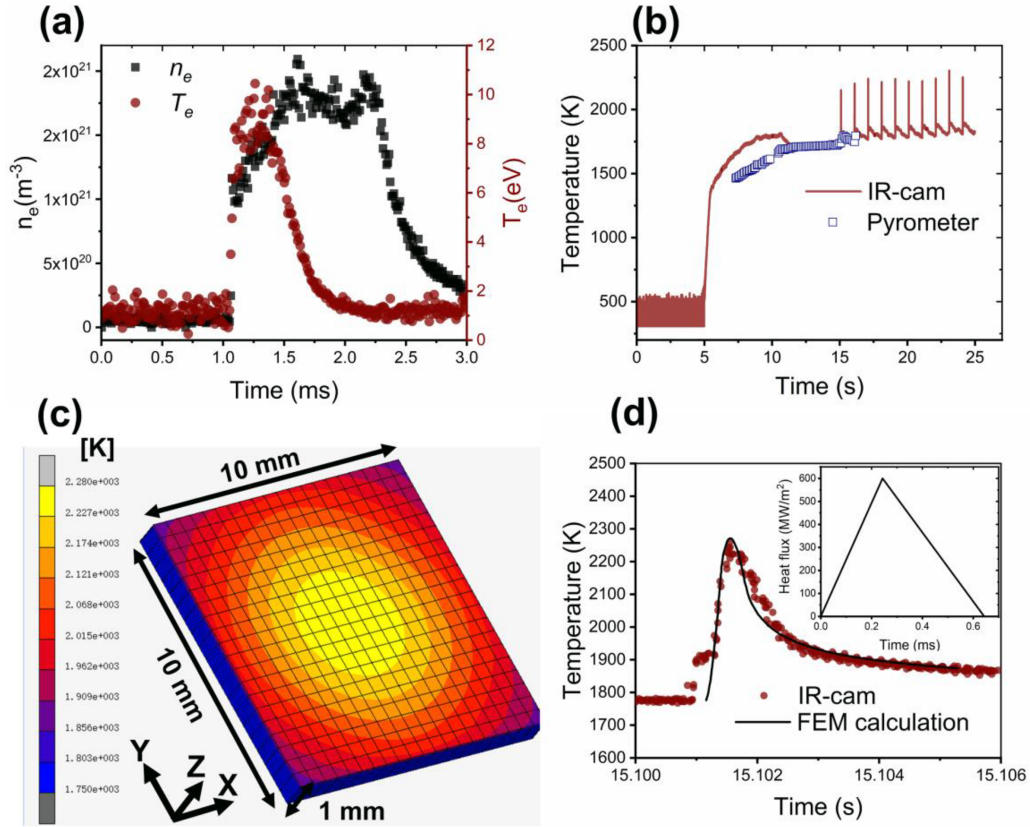
**Figure 1.** (*a*) Typical electron density ($n_e$) and temperature ($T_e$) profile during pulsed plasma measured by time-resolved Thomson scattering. (*b*) The thermographic profile of sample W1 recorded at the beam-spot center by the IR camera and pyrometer. (*c*) The 3D FEM model geometry, mesh, and the obtained peak temperature distribution. (*d*) The reconstructed temperature profile from IR camera measurements and the corresponding FEM calculation. The derived heat flux profile is shown in the inset, which is triangular with a rise time of 0.24 ms, a decay time of 0.4 ms and a peak value of 600 MW m$^{-2}$.

## 3. Microstructural results

### 3.1. Surface modifications

Figure 2 shows secondary electron images of the three tungsten grades before and after hydrogen plasma exposure as indicated in the figure. Figure 2(*a*) is hot-rolled tungsten with a non-uniform grain structure, where the elongation of the grains on the surface indicates the rolling direction. After plasma exposure (W1), as shown in figure 2(*d*), roughening of the surface was observed but no apparent crack was found. For the W-2%Y$_2$O$_3$ composite (WY1), the pristine microstructure contains equiaxed grains embedded with Y$_2$O$_3$ particles, which are mostly distributed along tungsten grain boundaries. For this sample, it is apparent that, after plasma exposure, the surface is full of microcracks. The grain boundaries are no longer clear, but it can be observed that the material volume enclosed by micro-cracks is of similar size as the original tungsten grains. Hence, it can be inferred that cracks nucleated predominantly at grain boundaries. Sample WT1 is like WY1, except that it has a smaller pristine grain size and consequently fine and dense microcracks, as shown in figures 2(*c*) and (*f*).

The role of the pulse number and the base temperature was investigated next. Firstly, keeping the same plasma parameters while increasing the pulse frequency to 5 Hz, 5000 pulses were applied. The results are shown in the first row of figure 3, with the same tungsten grades as ordered in figure 2. For sample W2, a crack network is formed due to the increased pulse numbers, along with exacerbated roughening. For WY2 and WT2, extra modifications were not significant, at least as visible from the surface. Secondly, increasing the base surface temperature to 2224 K, while limiting the number of pulses to 1000, showed different results. As shown in the second row of figure 3, all samples formed long cracks. For W3, a long straight crack developed in the sample center without much roughening. An overview at a lower magnification can be seen in figure 10(*b*). This contrasts with that of W1, which showed intense roughening but no cracks. For WY3 and WT3, long cracks (insets in figures 3(*e*) and (*f*)) also developed along with dense micro-cracks. Additional grain growth was observed, which becomes apparent when comparing to WY1 and WT1 (figures 2(*b*) and (*c*)).

### 3.2. Crack nucleation and propagation

We are particularly interested in the fracture behavior which poses a threat to the long-term performance of PFCs. From the surface analysis, it was already obvious that pure tungsten
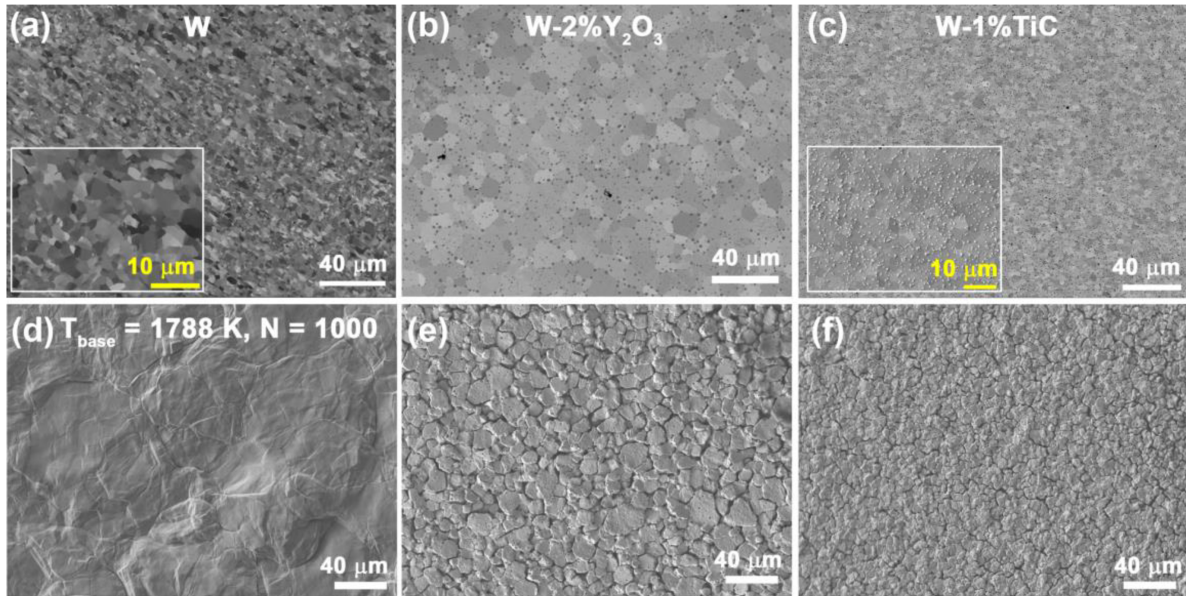
**Figure 2.** SEM images of sample W1 (pure W), WY1 (W-2%Y$_2$O$_3$) and WT1 (W-1%TiC) before (first row) and after plasma exposure (second row), respectively. The plasma exposure in the second row is at a base surface temperature of 1788 K, a peak transient heat flux of 600 MW m$^{-2}$, and a pulse number of 1000. Images are all taken from the center of the samples.
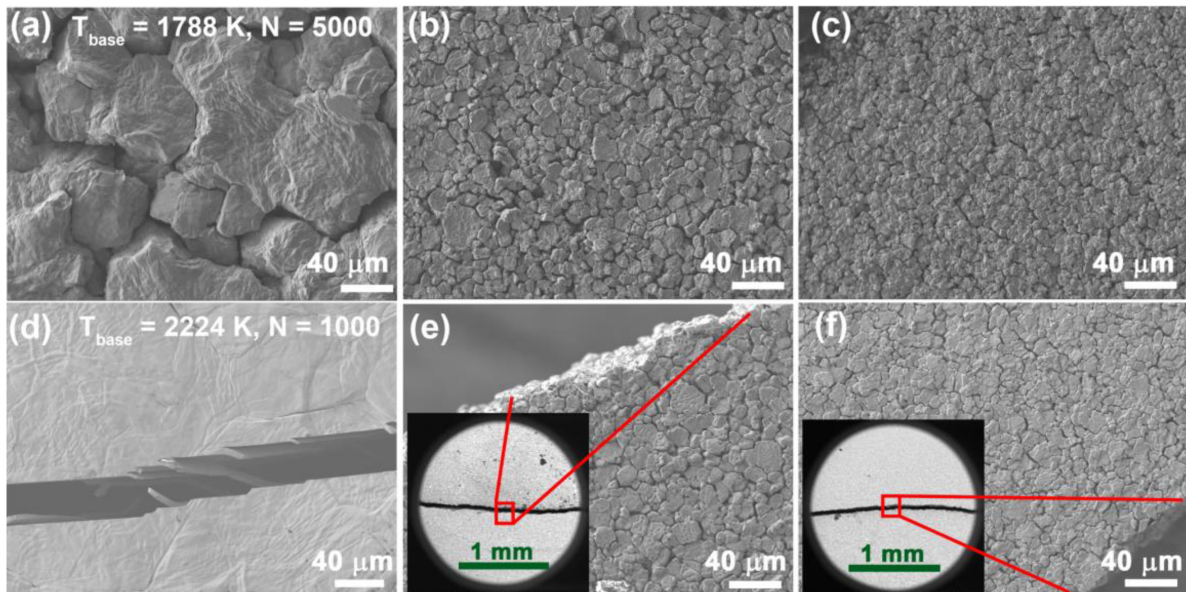


**Figure 3.** SEM images of (*a*) W2 (pure W), (*b*) WY2 (W-2%Y$_2$O$_3$), (*c*) WT2 (W-1%TiC), (*d*) W3 (pure W), (*e*) WY3 (W-2%Y$_2$O$_3$) and (*f*) WT3 (W-1%TiC), respectively. The edges in (*e*) and (*f*) are edges from the central long cracks as indicated by the insets. Images are all taken from the center of the samples.

behaves rather differently than the two composites. A detailed comparison is presented in figure 4. For pure tungsten, as shown in figure 4(*a*), intense slip bands were observed in front of a grain boundary. W3 is shown instead of W1 because only W3 formed natural long cracks such that the fine fracture morphology was not influenced by the external force applied to slice the samples for SEM analyses. For the two composites, microcracks occurred at grain boundaries, which can be associated with ceramic particles (e.g. interface decohesion), as highlighted in figures 4(*b*) and (*c*).

The cross-section fracture surfaces of all exposed samples were then examined, as shown in figures 5 and 6. All the cross-section micrographs show a damaged surface layer, which is associated with grain growth and microcracks, as highlighted in the images. Figure 6(*a*) shows 10 radial pictures of sample W3, overlaid to give an overview of the cross-section fracture surface, as this sample developed a radial crack ~18 mm long. An extensive recrystallization zone can be seen in the center, with a flat fracture surface. Next to it, the fracture mode is intergranular, extending radially ~5 mm
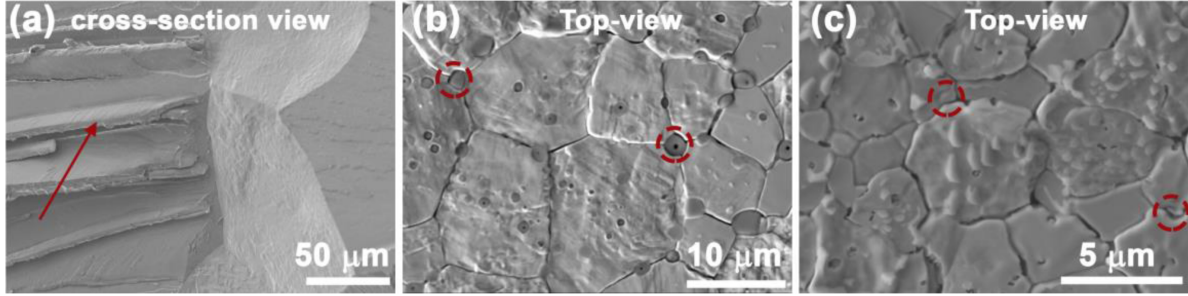
**Figure 4.** Fracture morphology of (*a*) W3 (pure W), (*b*) WY1 (W-2%Y$_2$O$_3$), and (*c*) WT1 (W-1%TiC), respectively. (*a*) Is the fracture surface while (*b*) and (*c*) are taken from the top surface but 3 mm away from the beam-spot center to avoid excessive roughening.

away from the beam-spot center. Beyond that, the fracture surface becomes flat again. A zoom-in image of this fracture mode transition region is shown in figure 6(*b*). For the two composites, figures 6(*c*) and (*d*), the damaged surface layer is shallower, showing the effect of ceramic particles in stabilizing the microstructure, which is consistent with the observations in figure 5. Figure 7 summarizes the surface crack length of the samples except W1 and W3. For the former, no surface crack forms and for the latter, the deep crack has overshadowed such evidence.

## 4. Discussion

The microstructural results have revealed some important features of the fracture behavior, which will now be analyzed with the aid of numerical simulations.

### 4.1. Surface crack formation

Firstly, in figure 2, it was found that the two tungsten-based composites had a lower cracking resistance than pure tungsten. Moreover, for pure tungsten, figures 2(*d*) and 3(*a*) reveal that surface cracks only appeared after multiple cycles, suggesting that crack initiation is driven by accumulated plastic strain. The yield strength of the studied tungsten-based composites was measured in [48] up to 600 °C (shown in appendix A). Pure tungsten has a slightly higher yield strength than the two composites, which could be related to the different degrees of cold working during fabrication. If the same trend in yield strength holds up to high temperatures in this study, pure tungsten would have accumulated less plastic strain than the two composite counterparts under the same thermal loading. In that case, pure tungsten is less susceptible to crack initiation, consistent with the experimental observation. Furthermore, the grain boundaries and phase interfaces could also have played a role in accommodating the accumulated plastic strain. As shown in figure 4(*a*), this is manifested as slip bands in front of the grain boundary. The grain boundaries maintain stress equilibrium/strain compatibility before fracture, for example, by slip transfer across the grain boundaries [49] and grain boundary sliding [50]. In contrast, for the composites, the presence of ceramic particles could suppress slip transfer and enhance stress concentration [51], leading to earlier fracture, as shown in figures 4(*b*) and (*c*).

The penetration depth of these surface cracks is of importance. Figure 7 summarizes the surface crack depth of the various samples tested in this study. The order of the specimens along the *x*-axis reveals an ascending crack depth distribution: the composition of the material is W-1%TiC, W-2%Y$_2$O$_3$, and pure W, respectively. For the same material composition, increasing pulse numbers appear first, followed by increasing base surface temperatures. A stabilized microstructure inhibits surface crack formation (WT < WY < W), whereas a high surface temperature promotes the surface crack formation. The surface crack depth was observed to depend on the number of pulses, but the effect is limited.

A predictive numerical analysis of the observed surface cracking behavior within the current theoretical framework of fatigue remains challenging [52]. Some numerical analyses on tungsten can be found in [53–57]. However, the output results rely on the assumed constitutive laws, for example, the Johnson-Cook model [58] at the continuum scale or a crystal plasticity model [59, 60]. Moreover, the high-flux hydrogen plasma and progressive dynamic recrystallization, which is relevant to the here applied experimental conditions as well as the ITER, affects the microstructure. Consequently, its effect, on the plastic deformation laws remains to be established. Moreover, special care should be taken while applying a specific type of fatigue model, as these models are mostly based on laboratory tensile tests where the loading condition and stress state are significantly different from the current study and those used in ITER.

Alternatively, we attempt to develop a simple analytical model to estimate the surface crack depth *d*. We hypothesize that *d* is proportional to the characteristic heat propagation distance of the transient heat load into the surface, which takes the following expression for a semi–infinite substrate,

$$L = \left( \frac{2\kappa t}{\rho c} \right)^{\frac{1}{2}}, \tag{7}$$

where $\kappa$ is the thermal conductivity, $t$ the pulse duration, $\rho$ the density and $c$ the specific heat capacity. $L$ can be interpreted as the root-mean-square-displacement from a random walk model of diffusion [61], which essentially means the average distance that a pulsed heat flux travels. Further, we postulate that $d$ is proportional to the power density inducing the temperature excursion ($\Delta T$), acting as a driving force for crack formation through the thermal stress, depending on the thermal
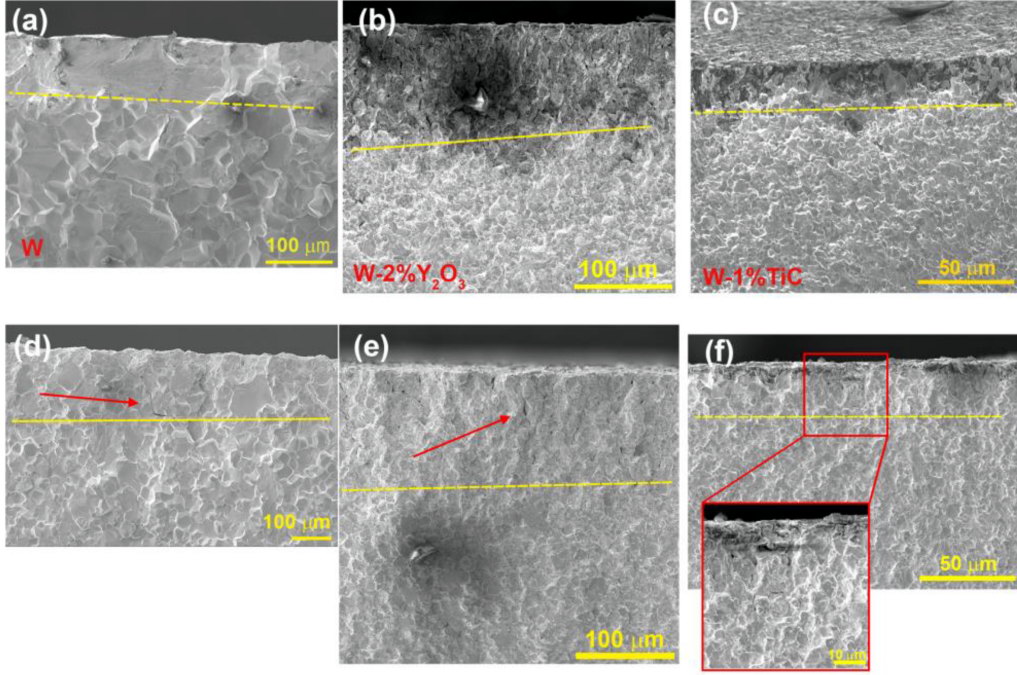
**Figure 5.** Cross-section fracture surfaces of sample (*a*) W1, (*b*) WY1, (*c*) WT1, (*d*) W2, (*e*) WY2, and (*f*) WT2 respectively, where the damaged surface layers are highlighted. The damaged surface layer is defined as the region with a morphology contrast with the matrix due to recrystallization, microcracks and fracture mode (cleavage vs. intergranular). More descriptions can be found in the text.
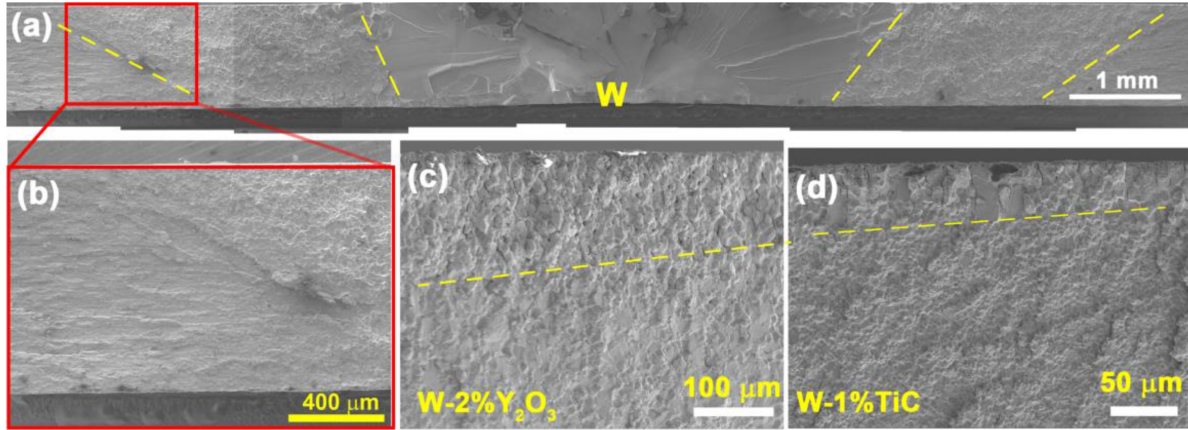


**Figure 6.** Cross-section fracture surfaces of (*a*)–(*b*) sample W3 (pure tungsten), (*c*) WY3 (W-2%Y$_2$O$_3$), and (*d*) WT3 (W-1%TiC), respectively. (*a*) Stitched 10 radial pictures. (*b*) Magnification of the highlighted region in (*a*). (*c*) and (*d*) are taken from the sample center.

expansion coefficient $\alpha$ and the Young's modulus $E$. The crack depth is also inversely proportional to the yield strength $\sigma_y$, measuring the resistance to crack initiation. Therefore, $d$ can be expressed as,

$$d = \beta \frac{\alpha E}{\sigma_y} \Delta T L = \beta \frac{\alpha E}{\sigma_y} \Delta T \left( \frac{2\kappa t}{\rho c} \right)^{\frac{1}{2}}, \tag{8}$$

where $\beta$ is a dimensionless parameter to be determined later. Here, $\Delta T$ is used instead of power density because $\Delta T$ not only depends on the power density but also on the shape of the pulse. It therefore better characterizes the driving force for material damage, as pointed out in [62]. For top-hat and triangular pulse shapes, which are typical for ELMs, analytical solutions of $\Delta T$ are at reach [63, 64]. For simplicity, the

influence of the pulse number $N$ is ignored. $d$ is dependent on the base temperature of the material as the thermo-mechanical properties in equation (8) are temperature-dependent. The temperature-dependent thermal conductivity $\kappa$, specific heat capacity $c$, thermal expansion coefficient $\alpha$ and the Young's modulus $E$ were taken from [46, 47, 65, 66], respectively (shown in appendix B).

$\beta$ is assumed to be temperature-independent and can be established by fitting equation (8) to experimental data. For this purpose, it is desirable to choose test conditions with a large pulse number $N$ to reduce the $N$ dependence and a time-independent $\sigma_y$. The latter criterion is not straightforward as while many experiments are performed at a base surface temperature below the recrystallization temperature
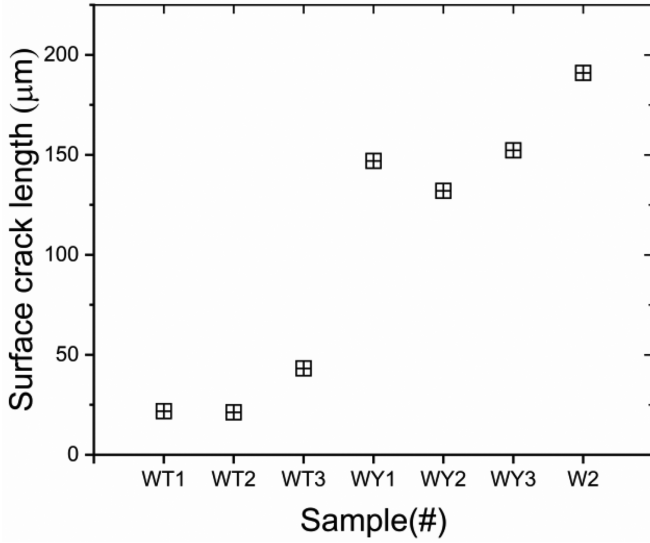
**Figure 7.** Surface crack length into the material of the different samples. The order of the specimens along the *x*-axis gives an ascending trend of the surface crack length and as discussed in the text.

**Table 2.** The testing conditions used in [4] for ITER-grade tungsten where $T_{base}$ is the base surface temperature, $\Delta T$ the peak temperature increase, and $t$ the pulse duration.
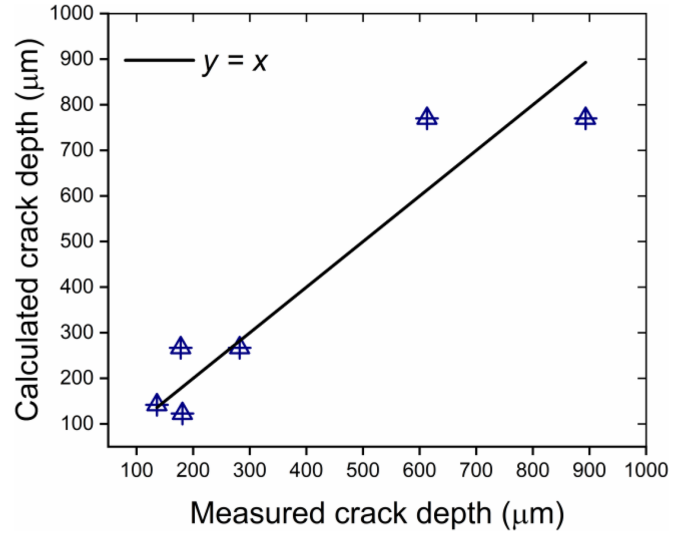
| Measured crack depth ($\mu$m)[a] | Calculated crack depth ($\mu$m) | $T_{base}$ (K) | $\Delta T$ (K) | $t$ (ms) | Yield strength (MPa)[b] |
|---|---|---|---|---|---|
| 178 | 267 | | 282 | | |
| 893 | 770 | | 815 | | |
| 282 | 267 | 1773 | 282 | | 55 |
| 613 | 770 | | 815 | 0.48 | |
| 136 | 142 | | 150 | | |
| 181 | 123 | 1473 | 150 | | 64 |

[a]The average crack depth is used.
[b]The yield strength is taken from the ITER materials handbook (v3.3) in recrystallized condition for $T_{base}$. Its dependence on $\Delta T$ is ignored as the influence of $\Delta T$ (a length scale characterized by $L$) is small at the crack front (a distance $d$ away from the surface). Therefore, the yield strength is determined by $T_{base}$ only.

of tungsten, the peak temperature increase $\Delta T$ can be above the recrystallization temperature and results in a partially recrystallized surface layer with a yield strength evolving with time. To circumvent this scenario, we used the data set reported by Loewenhoff *et al* [4] at a pulse number of $10^5$ and a base surface temperature of 1473 K and 1773 K of ITER-grade tungsten, where the recrystallization kinetics is fast enough to assume full recrystallization of the cracked surface layer. The experimental conditions are summarized in table 2.

Figure 8 shows the measured crack depth from [4] vs. the calculated crack depth using equation (8) for $\beta = 0.14$, where a reasonable agreement is obtained. Improvements can be achieved based on more measurements in the future, which are unfortunately scarce now. However, the main idea here is to estimate the surface crack depth incorporating relevant physics and mechanics, not to accurately model it. Moreover, we did not examine the validity of equation (8) for the two composites



**Figure 8.** The calculated surface crack depth using equation (8) for $\beta = 0.14$ vs. the measured surface crack depth from [4]. For a given symbol, the measured crack depth is from [4] and the calculated crack depth according to equation (8). The data are also given in table 2. The solid line is $y = x$.
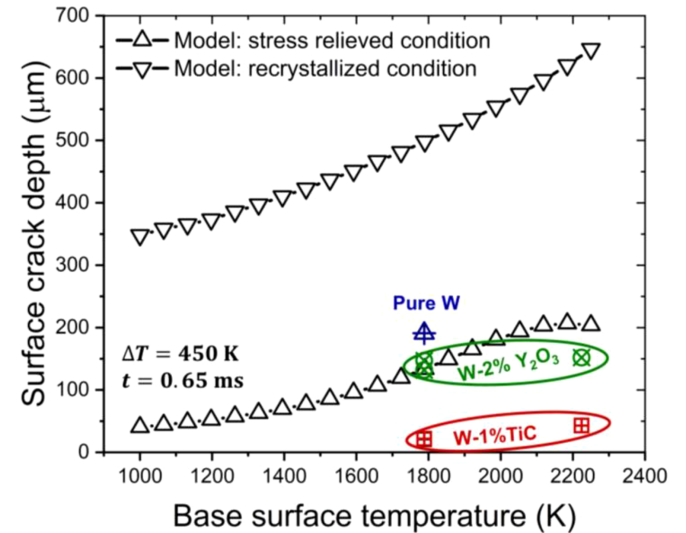


**Figure 9.** The calculated surface crack depth using equation (8) as a function of the base surface temperature ($T_{base}$) with a peak temperature increase ($\Delta T$) of 450 K, a pulse duration ($t$) of 0.65 ms, and yield strength ($\sigma_y$) of ITER-grade tungsten under stress relieved and recrystallized conditions. The measured surface crack depth in this study is also displayed.

due to the lack of the corresponding thermo-mechanical properties. Note that to test equation (8) for the composites, it requires experiments performed under a large pulse number $N$ and a time-independent $\sigma_y$, as for the pure tungsten case.

Using the fitted $\beta$ from figure 8, the analytical model expressed by equation (8) is plotted as a function of the base surface temperature ($T_{base}$) with $\Delta T = 450$ K, $t = 0.65$ ms and $\sigma_y$ in stressed relieved and recrystallized conditions of ITER-grade tungsten (given in appendix C) in figure 9. As can be seen, the $\sigma_y$ has a strong influence on the surface crack depth,
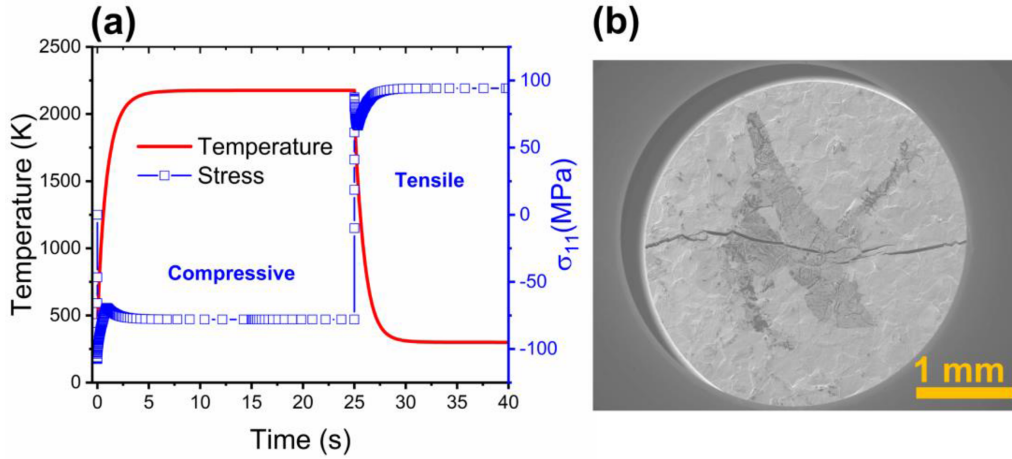
**Figure 10.** (*a*) The simulated thermal stress of sample W3 corresponding to the steady-state heating-holding-cooling temperature profile. (*b*) The corresponding fracture surface image at low magnification with the biaxial stress state illustration.

as $\sigma_y$ declines with increasing base surface temperature, which prevails the other temperature-dependent terms in equation (8) (e.g. $E$ decreases with temperature), and with the fraction of recrystallization.

The results shown in figure 7 are now rearranged in figure 9 as well to allow a better interpretation. Here, the modeled surface crack depth of the ITER-grade pure tungsten in stress relieved and recrystallized conditions act as two extreme cases. Since the studied tungsten-based composites were partially recrystallized by the combined heat loads, their crack depths are expected to be bounded by the modeled results. It is seen that the surface fracture depth of pure W and W-2%Y$_2$O$_3$ can be reasonably described by the modeled case for the stress relieved ITER-grade tungsten. The small deviations may be related to partial recrystallization (e.g. the pure tungsten case) or the thermal stress relief by the micro-cracks presented in the surface layer, providing expansion channels (e.g. the W-2%Y$_2$O$_3$ case). However, W-1%TiC consistently shows better crack resistance than the other two counterparts, which may be related to its different phase boundary structures between the TiC ceramic particle and the W matrix [48], not captured by our simple model. Furthermore, the observed particle-matrix interface decohesion for the two composites may be relevant but was not considered. Still, this model calibrated from pure tungsten would provide an upper bound estimate of the surface crack depth due to the transient heat loads.

### 4.2. Deep crack formation

The formation of deep cracks (> 600 $\mu$m, the maximum surface crack depth estimated by the analytical model) for samples exposed at a base surface temperature of 2224 K is addressed next.

Let us consider the thermal stress due to the steady-state heat flux with a thermo-mechanical finite element analysis. The analysis is also performed in MSC.Marc/Mentat® based on the thermal model described in section 2.4. As for the mechanical boundary conditions, no displacement in the *z*-direction is allowed for the bottom nodes and the displacement in the surface normal directions of the sides are also constrained.

The temperature-dependent Young's modulus, Poisson's ratio, and thermal expansion coefficient for tungsten are taken from [65, 66] (given in appendix B). The temperature-dependent yield strength of tungsten in a recrystallized condition from the ITER materials handbook (v3.3) is adopted since extensive recrystallization has occurred for sample W3 (given in appendix C). The von Mises yield criterion is used. Perfect plasticity is assumed here because of a lack of a generalized hardening law in the studied temperature range. This approximation is not expected to influence the conclusions of this study.

Figure 10(*a*) shows the simulated thermal stress corresponding to a typical heating-holding-cooling temperature profile using the developed thermo-mechanical FEM model. The calculated thermal stress is biaxial ($\sigma_{11} = \sigma_{22}$, while other stress components are negligible), and compressive during heating and tensile during cooling, consistent with a previous study [34]. Combined with the crack path shown in figure 10(*b*) (the opening fracture mode [67]), one would expect that it is the tensile stress during the final cooling stage that induces crack propagation. This conclusion is supported by the radially graded surface fracture morphology shown in figures 6(*a*) and 6(*b*), where a transition from ductile intergranular fracture in the middle to brittle cleavage fracture at the edge can be seen. This transition point is around 5 mm away from the center and has a surface temperature of ~1000 K during steady-state plasma loading. If we assume the fracture morphology transition is controlled by temperature [68], known as the brittle-to-ductile transition temperature, which is ~300–650 K for single crystal tungsten [69], such a graded fracture surface could only have been formed during the cooling stage. The observed cleavage fracture and intergranular fracture surface are very similar to what has been reported in Ref [68]. This process is aided by the presence of surface cracks due to cyclic transient heat loading. Here, the range of the thermal stress due to the transient and steady-state heat flux should be distinguished. For the former, it is limited to the surface layer, as estimated by equation (8). The surface cracks, therefore, serve to relieve the subsequent cycles of transient thermal stress, as shown in figure 7. For the latter,

it is present in the material bulk and would be intensified at the surface crack tip. For example, the stress intensity factor is proportional to the square root of the crack length in a linear elastic fracture mechanics analysis [67]. For an elastic analysis and a crack length ($a$) of 536 $\mu$m, as predicted by the analytical model, the far-field stress ($\sigma$) would equal 133 MPa, as calculated in figure 10($a$) (multiplied with a factor of $\sqrt{2}$ to account for the biaxial stress state). The resulting stress intensity factor is then equal to $K = \sigma\sqrt{\pi a} = 9.19$ MPa$\cdot$m$^{\frac{1}{2}}$, which is larger than the fracture toughness of pure tungsten $\left(2.7 \pm 0.2 \text{ MPa} \cdot \text{m}^{\frac{1}{2}}\right)$ determined at a cryogenic temperature [69], suggesting the above process is kinetically possible. The above discussion is mostly for pure tungsten (sample W3) as the mechanical properties of pure tungsten are relatively well documented in the literature. However, since the two composites (insets in figures 3($e$) and ($f$)) also developed long cracks through the thickness, the proposed fracture picture analysis may be general.

Finally, the high-flux hydrogen plasma could also have contributed to the above process in addition to the heat load it delivered. Hydrogen-mediated plasticity and fracture are widely reported [11, 70–73], which might explain the observed synergetic effect [29, 74]. However, such an effect could not be disentangled in the current study because of the lack of proper dummy tests (e.g. same heat flux but with and without the hydrogen particle flux), which is nontrivial. Therefore, more dedicated experiments are ongoing to reveal the role of hydrogen on the mechanical behavior of tungsten.

## 5. Conclusion and outlook

Hot-rolled tungsten, and PIM W-1%TiC and W-2%Y$_2$O$_3$ composites were exposed to combined steady-state/transient hydrogen plasma up to a base surface temperature of 2224 K, and up to 5000 transient pulses for 1000 s in Magnum-PSI. Crack initiation and propagation behavior were studied. Combining microstructural characterization and thermo-mechanical numerical analyses, the failure phenomena are rationalized as follows:

(a) Transient heat load drives surface crack initiation. For pure tungsten, the surface crack depth can be estimated by a simple analytical model: $d = 0.14\frac{\alpha E}{\sigma_y}\Delta T\left(\frac{2\kappa t}{\rho c}\right)^{\frac{1}{2}}$. The surface crack depth of W-2%Y$_2$O$_3$ is slightly smaller than for pure tungsten while W-1%TiC shows much shallower surface cracking.

(b) The steady-state heat load induced tensile stresses open existing surface cracks.

(c) The above two stages are meditated by the microstructure. Ceramic particles stabilize the microstructure but promote surface crack initiation because of suppressed plasticity at grain boundaries and particle-matrix interfaces. Such surface cracks relieve the subsequent cycles of transient thermal stress but can intensify the steady-state thermal stress, hence promoting crack propagation.
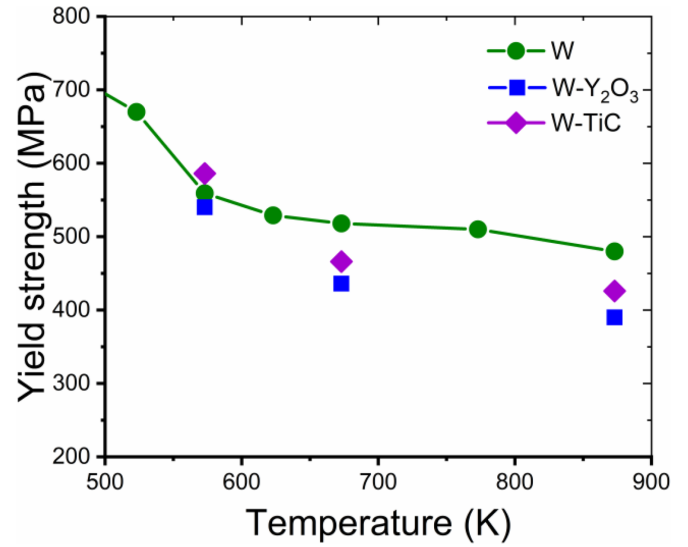


**Figure A.** Yield strength of pure tungsten, W-1%TiC and W-2%Y$_2$O$_3$ from [48].

The current study provides a mechanistic view of tungsten-based PFCs performance under extreme operation scenarios which suggests new testing procedures for evaluating the long-term thermo-mechanical performance of tungsten-based PFCs. For example, performing steady-state heat load cycles on pre-damaged tungsten monoblocks (with surface cracks) to monitor the surface crack propagation rate. However, an even deeper understanding of the underlying failure mechanism requires dedicated experiments and numerical analyses to disentangle the role of different constituents, for example, the effect of hydrogen on the mechanical behavior of tungsten.
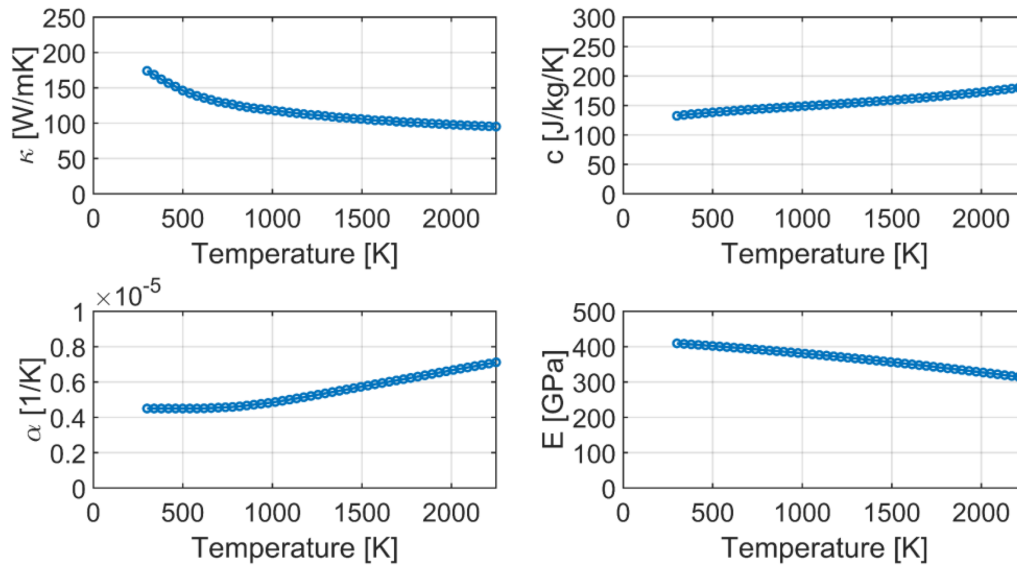
## Appendix A. Yield strength of the studied tungsten-based composites

## Appendix B. The temperature-dependent properties of pure tungsten

## Appendix C. Yield strength of ITER-grade tungsten

**Figure B.** The temperature-dependent thermal conductivity κ [46], specific heat capacity c [47], thermal expansion coefficient α [66] and the Young's modulus E [65] of pure tungsten, respectively.
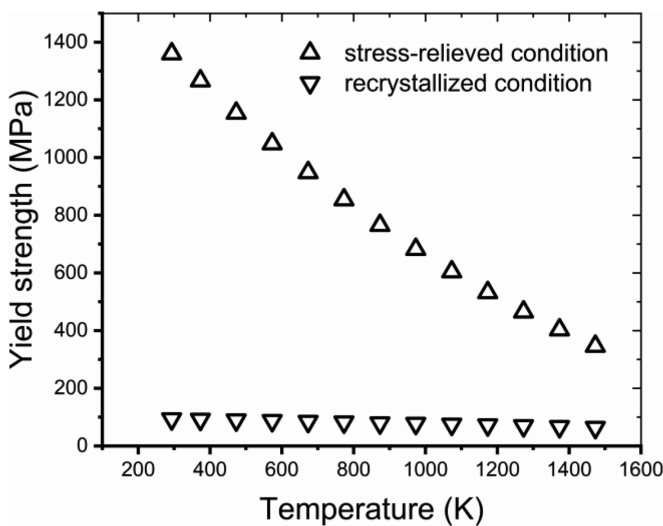


**Figure C.** Yield strength of ITER-grade tungsten from the ITER materials handbook (v3.3).

## ORCID iDs

T.W. Morgan https://orcid.org/0000-0002-5066-015X
J.A.W. Van Dommelen https://orcid.org/0000-0003-4029-0308
M. Rieth https://orcid.org/0000-0002-6231-6241
J.P.M. Hoefnagels https://orcid.org/0000-0001-8359-7575
G. De Temmerman https://orcid.org/0000-0002-4173-0961

## References

[1] Hall E. 1951 *Proc. Phys. Soc.* B **64** 747
[2] Ren C., Fang Z.Z., Xu L., Ligda J.P., Paramore J.D. and Butler B.G. 2019 *Acta Mater.* **162** 202
[3] Mannheim A., van Dommelen J.A.W. and Geers M.G.D. 2019 *Model. Simul. Mater. Sci. Eng.* **27** 065001
[4] Loewenhoff T. *et al* 2015 *Nucl. Fusion* **55** 123004
[5] Wirtz M., Uytdenhouwen I., Barabash V., Escourbiac F., Hirai T., Linke J., Th L., Panayotis S. and Pintsuk G. 2017 *Nucl. Fusion* **57** 066018
[6] Pitts R.A. *et al* 2019 *Nucl. Mater. Energy* 100696
[7] McDowell D.L. 1996 *Int. J. Fract.* **80** 103
[8] De Temmerman G., Hirai T. and Pitts R.A. 2018 *Plasma Phys. Control. Fusion* **60** 044018
[9] Loewenhoff T., Linke J., Pintsuk G. and Thomser C. 2012 *Fusion Eng. Des.* **87** 1201
[10] Wirtz M., Kreter A., Linke J., Loewenhoff T., Pintsuk G., Sergienko G., Steudel I., Unterberg B. and Wessel E. 2017 *Phys. Scr.* **T170** 014066
[11] Robertson I.M., Sofronis P., Nagao A., Martin M.L., Wang S., Gross D.W. and Nygren K.E. 2015 *Metall. Mater. Trans.* A **46** 2323
[12] Pitts R.A. *et al* 2013 *J. Nucl. Mater.* **438** S48
[13] Kurishita H., Amano Y., Kobayashi S., Nakai K., Arakawa H., Hiraoka Y., Takida T., Takebe K. and Matsui H. 2007 *J. Nucl. Mater.* **367–370** 1453
[14] Battabyal M., Schäublin R., Spätig P. and Baluc N. 2012 *Mater. Sci. Eng.* A **538** 53
[15] Pintsuk G., Blagoeva D. and Opschoor J. 2013 *J. Nucl. Mater.* **442** S282
[16] Xie Z.M., Liu R., Zhang T., Fang Q.F., Liu C.S., Liu X. and Luo G.N. 2016 *Mater. Des.* **107** 144
[17] Xie Z.M. *et al* 2017 *J. Nucl. Mater.* **496** 41
[18] Antusch S., Norajitra P., Piotter V. and Ritzhaupt-Kleissl H.J. 2011 *J. Nucl. Mater.* **417** 533
[19] De Temmerman G. *et al* 2013 *Fusion Eng. Des.* **88** 483
[20] Morgan T.W., de Kruif T.M., van der Meiden H.J., van den Berg M.A., Scholten J., Melissen W., Krijger B.J.M., Bardin S. and De Temmerman G. 2014 *Plasma Phys. Control. Fusion* **56** 095004
[21] Hirai T. and Pintsuk G. 2007 *Fusion Eng. Des.* **82** 389
[22] Linke J. *et al* 2011 *Nucl. Fusion* **51** 073017
[23] Loewenhoff T., Bürger A., Linke J., Pintsuk G., Schmidt A., Singheiser L. and Thomser C. 2011 *Phys. Scr.* **T145** 014057
[24] Pestchanyi S., Garkusha I. and Landman I. 2011 *Fusion Eng. Des.* **86** 1681

[25] Morgan T.W., Zielinski J.J., Hensen B.J., Xu H.Y., Marot L and De Temmerman G 2013 *J. Nucl. Mater.* **438** S784

[26] Pintsuk G., Bobin-Vastra I., Constans S., Gavila P., Rödig M. and Riccardi B. 2013 *Fusion Eng. Des.* **88** 1858

[27] Wirtz M., Linke J., Pintsuk G., De Temmerman G. and Wright G.M. 2013 *J. Nucl. Mater.* **443** 497

[28] Li M., Werner E. and You J.-H. 2015 *Nucl. Mater. Energy* **2** 1

[29] Wirtz M. *et al* 2015 *Nucl. Fusion* **55** 123017

[30] Yu J.H., De Temmerman G., Doerner R.P., Pitts R.A. and van den Berg M.A. 2015 *Nucl. Fusion* **55** 093027

[31] Wang L., Wang B., Li S.-D., Ma D., Tang Y.-H. and Yan H. 2016 *Int. J. Refract. Met. Hard Mater* **61** 61

[32] Yuan Y., Du J., Wirtz M., Luo G.N., Lu G.H. and Liu W. 2016 *Nucl. Fusion* **56** 036021

[33] Jia Y.Z., Liu W., Xu B., Qu S.L. and Morgan T.W. 2017 *J. Nucl. Mater.* **487** 68

[34] Li C., Zhu D., Li X., Wang B. and Chen J. 2017 *Nucl. Mater. Energy* **13** 68

[35] Brezinsek S. *et al* 2017 *Nucl. Fusion* **57** 116041

[36] Antusch S. *et al* 2015 *Nucl. Mater. Energy* **3–4** 22

[37] Manhard A., Matern G. and Balden M. 2013 *Pract. Metall.* **50** 5

[38] Zayachuk Y., Tanyeli I., Van Boxel S., Bystrov K., Morgan T.W. and Roberts S.G. 2016 *Nucl. Fusion* **56** 086007

[39] van der Meiden H.J. *et al* 2012 *Rev. Sci. Instrum.* **83** 123505

[40] van Eck H.J.N. *et al* 2019 *Fusion Eng. Des.* **142** 26

[41] Riemann K.U. 1991 *J. Phys. D Appl. Phys.* **24** 493

[42] van der Meiden H.J., Vernimmen J.W.M., Bystrov K., Jesko K., Kantor M.Y., De Temmerman G. and Morgan T.W. 2016 *Appl. Phys. Lett.* **109** 261102

[43] Westerhout J. 2010 Carbon chemical erosion in high flux and low temperature hydrogen plasma *PhD Thesis* Eindhoven University of Technology.

[44] Stangeby P.C. 2000 *The Plasma Boundary of Magnetic Fusion Devices* (Bristol: Institute of Physics Publishing)

[45] Zielinski J.J., van der Meiden H.J., Morgan T.W., T Hoen M.H.J., Schram D.C. and De Temmerman G. 2014 *Appl. Phys. Lett.* **104** 124102

[46] Ho C.Y., Powell R.W. and Liley P.E. 1972 *J. Phys. Chem. Ref. Data* **1** 279

[47] White G.K. and Collocott S.J. 1984 *J. Phys. Chem. Ref. Data* **13** 1251

[48] Yin C. *et al* 2018 *Int. J. Refract. Met. Hard Mater* **75** 153

[49] Lee T.C., Robertson I.M. and Birnbaum H.K. 1989 *Scr. Mater.* **23** 799

[50] Chawla K.K. 1973 *Philos. Mag.* **28** 401

[51] Biner S.B. 1996 *Acta Mater.* **44** 1813

[52] Pineau A., McDowell D.L., Busso E.P. and Antolovich S.D. 2016 *Acta Mater.* **107** 484

[53] Arakcheev A.S. *et al* 2015 *J. Nucl. Mater.* **463** 246

[54] Du J., Yuan Y., Wirtz M., Linke J., Liu W. and Greuner H. 2015 *J. Nucl. Mater.* **463** 219

[55] Li M., Werner E. and You J.-H. 2015 *Fusion Eng. Des.* **90** 88

[56] Li C., Zhu D., Wang B. and Chen J. 2018 *Fusion Eng. Des.* **132** 99

[57] Zinovev A., Terentyev D. and Delannay L. 2017 *Phys. Scr.* **2017** 014002

[58] Lennon A.M. and Ramesh K.T. 2000 *Mater. Sci. Eng.* A **276** 9

[59] Lim H., Battaile C.C., Carroll J.D., Boyce B.L. and Weinberger C.R. 2015 *J. Mech. Phys. Solids* **74** 80

[60] Terentyev D., Xiao X., Dubinko A., Bakaeva A. and Duan H. 2015 *J. Mech. Phys. Solids* **85** 1

[61] Sethna J. 2006 *Statistical Mechanics: Entropy, Order Parameters, and Complexity* (Oxford, New York: Oxford University Press)

[62] Yu J.H., De Temmerman G., Doerner R.P. and van den Berg M.A. 2016 *Phys. Scr.* **T167** 014033

[63] Carslaw H.S. and Jaeger J.C. 1959 Conduction of Heat in Solids 2nd edn (Oxford: Clarendon)

[64] Bäuerle D. 2013 *Laser Processing and Chemistry* (Springer Science & Business Media)

[65] Lowrie R. and Gonas A.M. 1967 *J. Appl. Phys.* **38** 4505

[66] Slack G.A. and Bartram S.F. 1975 *J. Appl. Phys.* **46** 89

[67] Chawla K.K. and Meyers M. 1999 *Mechanical Behavior of Materials* (Englewood Cliffs, NJ: Prentice-Hall)

[68] Habainy J., Iyengar S., Lee Y. and Dai Y. 2015 *J. Nucl. Mater.* **465** 438

[69] Giannattasio A. and Roberts S.G. 2007 *Philos. Mag.* **87** 2589

[70] Novak P., Yuan R., Somerday B.P., Sofronis P. and Ritchie R.O. 2010 *J. Mech. Phys. Solids* **58** 206

[71] Terentyev D., Dubinko A., Bakaeva A., De Temmerman G. and Unterberg B. 2017 *Phys. Scr.* **T170** 014064

[72] Depover T. and Verbeken K. 2018 *Int. J. Hydrogen Energy* **43** 3050

[73] Deng Y. and Barnoush A. 2018 *Acta Mater.* **142** 236

[74] van Eden G.G., Morgan T.W., van der Meiden H.J., Matejicek J., Chraska T., Wirtz M. and De Temmerman G. 2014 *Nucl. Fusion* **54** 123010